

Synergy in Commercial Brass Reinforced Carbon Hybrids Interlayer towards Highly Reversible Zn Anodes

Kun Rui,^{*[a]} Ke Chen,^[a] Yakai Chen,^[a] Wenhao Si,^[a] Jiliang Liu,^[a] Yan Yan,^[a] Huijuan Lin,^[a] Cong Zhao,^{*[b]} and Jixin Zhu^[c]

Aqueous Zn-ion batteries (AZIBs) have served as a promising candidate for next-generation energy storage applications. Nonetheless, interfacial issues concerning the metallic Zn anode including hydrogen evolution reaction (HER), chemical corrosion, and dendrite growth remain to be carefully addressed. Herein, we present a facile and cost-effective strategy to implant carbon nanotube (CNT) framework with a commercial brass alloy as the protective interlayer. The conductive network constructed by interconnected CNTs ensures an optimal electric field distribution over the entire electrode surface. The embedded brass alloy not only inhibits the aggregation of

CNTs, but also mitigates surface corrosion through its abundance of chemically inert Cu sites. Leveraging the synergy within the carbon hybrids featuring high Zn-affinity and abundant nucleation sites for Zn^{2+} , lowered energy barriers and promoted redox kinetics for Zn deposition enable highly stabilized and reversible Zn anodes. As a result, symmetric cells demonstrate extended cycling lifespan of 3000 h and 1200 h at 2 mA cm^{-2} and 5 mA cm^{-2} for 1 mAh cm^{-2} , respectively. Furthermore, the optimized Zn| MnO_2 full cells exhibit impressive cycling stability for 1000 cycles at 2 A g^{-1} .

Introduction

Aqueous Zn-ion batteries (AZIBs) have served as a promising candidate for next-generation energy storage applications, benefitting from the notable advantages of Zn metal including considerably high gravimetric and volumetric capacities (i.e. 820 mAh g^{-1} and 5850 mAh cm^{-3}), a relatively low redox potential (-0.762 V vs. standard hydrogen electrode), and environmental friendliness.^[1] Owing to the intrinsic safety and resource abundance, cost-benefit Zn electrochemistry is highly attractive as an alternative solution to the existing Li-based systems, particularly for integrating intermittent power generation into future grids.^[2] Yet, issues concerning the metallic Zn anode such as hydrogen evolution reaction (HER), chemical corrosion, and dendrite growth remain to be addressed. Otherwise, inferior cycling stability and battery failure due to short circuits still have impeded the practical application of AZIBs.

To date, great progress has been made to address the aforementioned challenges, including 3D structured host

design,^[3] electrolyte modification,^[4] separator modification,^[5] etc. Yet, achieving continuous and sustained regulation of the Zn deposition behavior and inhibition of side reactions remains quite challenging. While sacrifice of ionic conductivity occurs when introducing electrolyte additives, aggravated HER tendency requires renewed attention in terms of enlarged surface active sites within 3D hosts. On the other hand, the introduction of interface layer has shown substantial promise in stabilizing the Zn anode.^[6] By preventing direct contact between the Zn anode and the electrolyte, these layers significantly inhibit side reactions. Additionally, the interfacial layer featuring desired mechanical properties can effectively suppress volume expansion and Zn dendrite growth. Various species with strong Zn affinity such as metallic Au/Ag/In,^[7] ZrO_2 ,^[8] and metal-organic frameworks (MOFs) or covalent organic frameworks (COFs),^[9] have been applied to construct interfacial layers. Occasionally, complex methods or expensive equipment such as 3D printing, magnetron sputtering, and atomic layer deposition were involved,^[10] posing challenges towards practical applications.

Carbonaceous materials have offered new possibilities for stabilizing Zn anode owing to their advantageous properties such as scalability, diverse forms, lightweight nature, and high electric conductivity.^[11] In particular, carbon nanotubes (CNTs) have demonstrated great promise for reducing the migration barrier of Zn^{2+} as well as regulating the electric field.^[12] For instance, Hu et al. prepared a bulk-phase composite anode of CNTs with Zn powders by a powder-metallurgy-based strategy,^[13] where CNTs reinforced uniform distribution at the grain boundaries. Besides, doped CNTs provided numerous nucleation sites for Zn plating on the top layer within the sequentially coated graphene/CNTs interlayer.^[14] However, establishing well-defined charge transfer pathways with highly dispersive CNTs, while overcoming their natural tendency to aggregate, remains challenging, especially in a straightforward

[a] K. Rui, K. Chen, Y. Chen, W. Si, J. Liu, Y. Yan, H. Lin
School of Flexible Electronics (Future Technologies), Institute of Advanced Materials (IAM), Key Laboratory of Flexible Electronics (KLOFE), Nanjing Tech University (NanjingTech), 30 South Puzhu Road, Nanjing 211816, P. R. China
E-mail: iamkrui@njtech.edu.cn

[b] C. Zhao
College of Mechanical and Electrical Engineering, Nanjing University of Aeronautics and Astronautics, 29 Yudao Street, Nanjing 210016, P. R. China
E-mail: zhaocong_ccme@nuaa.edu.cn

[c] J. Zhu
State Key Laboratory of Fire Science, University of Science and Technology of China, 443 Huangshan Road, Hefei 230027, P. R. China

 Supporting information for this article is available on the WWW under <https://doi.org/10.1002/batt.202400792>

and cost-effective manner. More importantly, rational incorporation of inexpensive species with high Zn affinity to construct carbon hybrids interlayer offers further opportunities for enhancing Zn electrochemistry.

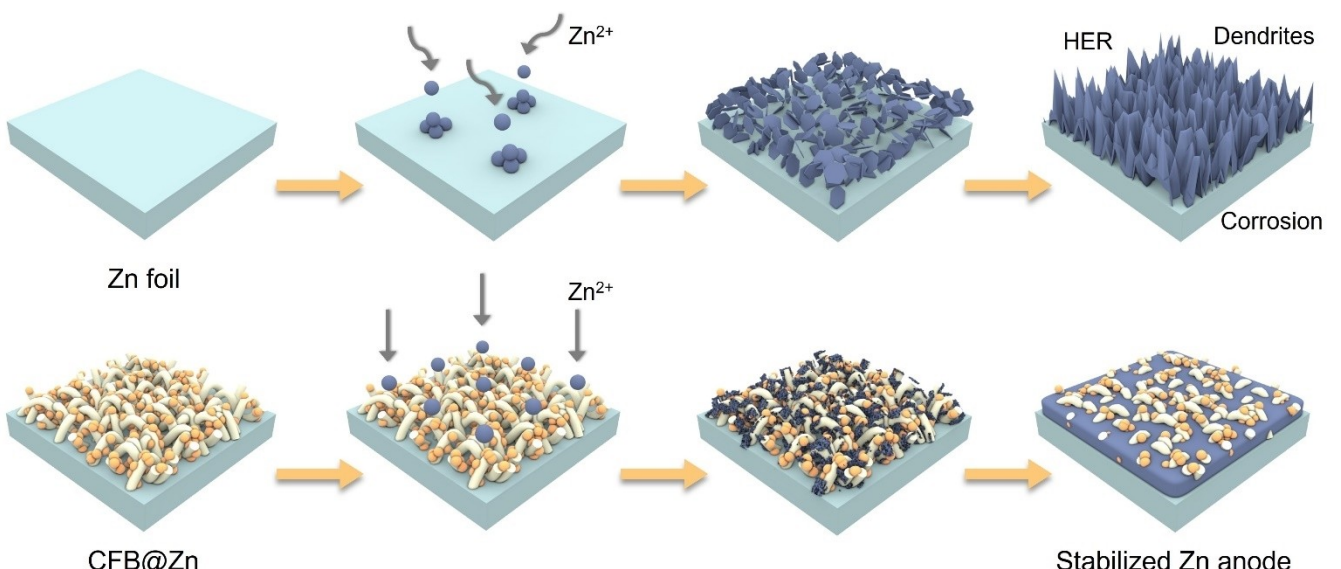
More recently, plenty of alloys designed to resist chemical corruptions (e.g., Zn–Cu, Zn–Al, Zn–Se, etc.) have exhibited high binding energy with Zn atoms, as confirmed by both theoretical calculations and experimental results.^[15] To this end, CNTs framework integrated with a commercial brass alloy was introduced as the protective layer over the Zn anode (CFB@Zn) via a facile and scalable solvent casting strategy. The conductive network constructed by interconnected CNTs ensured desired electric field distribution over the entire electrode surface. The presence of embedded brass alloy effectively inhibited CNT aggregation and more importantly, suppressed the chemical corrosion with the electrolyte. Benefiting from the high Zn-affinity of homogeneously distributed brass alloy, abundant nucleation sites for Zn^{2+} enabled lowered energy barriers for Zn deposition. As a result, the symmetric cells based on CFB@Zn anodes delivered extended cycling life of 3000 h and 1200 h at 2 mA cm^{-2} and 5 mA cm^{-2} for 1 mAh cm^{-2} , respectively. Furthermore, the CFB@Zn | | MnO_2 full cell exhibited impressive cycling stability for 1000 cycles at 2 A g^{-1} .

Results and Discussion

The CFB protective layer was constructed on the surface of Zn anode via a simple scraping method. As illustrated by the schematic diagrams in Scheme 1, the presence of CFB interface layer prevented the direct contact between the Zn anode and the electrolyte, alleviating side reaction issues such as HER and surface corrosion. More importantly, the CFB interface layer benefitted from the high Zn-affinity of homogeneously distributed brass alloy, providing abundant nucleation sites for

Zn^{2+} with lowered energy barriers. Meanwhile, the conductive network constructed by interconnected CNTs ensured desired electric field distribution over the entire electrode surface. Therefore, the synergy of the engineered interface enabled stabilized and dendrite-free Zn anodes. The surface morphology of as-obtained CFB@Zn anode was first revealed by scanning electron microscopy (SEM). While bare Zn exhibited scratches or folds due to the manufacture or pre-treatment process (Figure S1), CFB@Zn anode was covered with small particles at a lower magnification (Figure 1a). Specifically, brass alloy particles ranging from 100 to 200 nm were uniformly distributed within the interconnected CNTs network (Figure 1b), establishing a 3D conductive framework decorated with abundant zincophilic sites. The top-view energy dispersive X-ray spectroscopy (EDS) elemental mapping suggested the homogeneous distribution of C, Cu and Zn (Figure S2). The dense interfacial layer was also observed from the side-view SEM image in Figure 1c. By contrast, unnested brass alloy was also coated on the surface of Zn anode with the PVDF binder (Brass@Zn). As seen in Figure S3, severe agglomeration of brass alloy particles was noticed without the presence of CNT matrix, leaving irregular voids and pores within the interlayer and even uncovered Zn surfaces from both of the top and side views. The significant difference in appearance at the macro level also suggested the dense and uniform feature of CFB@Zn (Figure S4).

X-ray diffraction (XRD) and X-ray photoelectron spectroscopy (XPS) were also employed to reveal the chemical composition of the artificial layer. In Figure 1d, the brass powders exhibited strong diffraction peaks at around 43° , 63° and 79° , corresponding to (110), (200), and (211) facets of the cubic CuZn with the space group of Pm-3m (221). Moreover, CFB@Zn exhibited identical characteristic peaks to bare Zn (Figure S5). The full XPS survey spectrum confirmed the co-existence of C, Cu and Zn in the artificial layer (Figure S6). The characteristic peaks at 932.5 and 952.2 eV in the high-resolution



Scheme 1. Schematic illustration of Zn^{2+} deposition on bare Zn foil and CFB@Zn anodes.

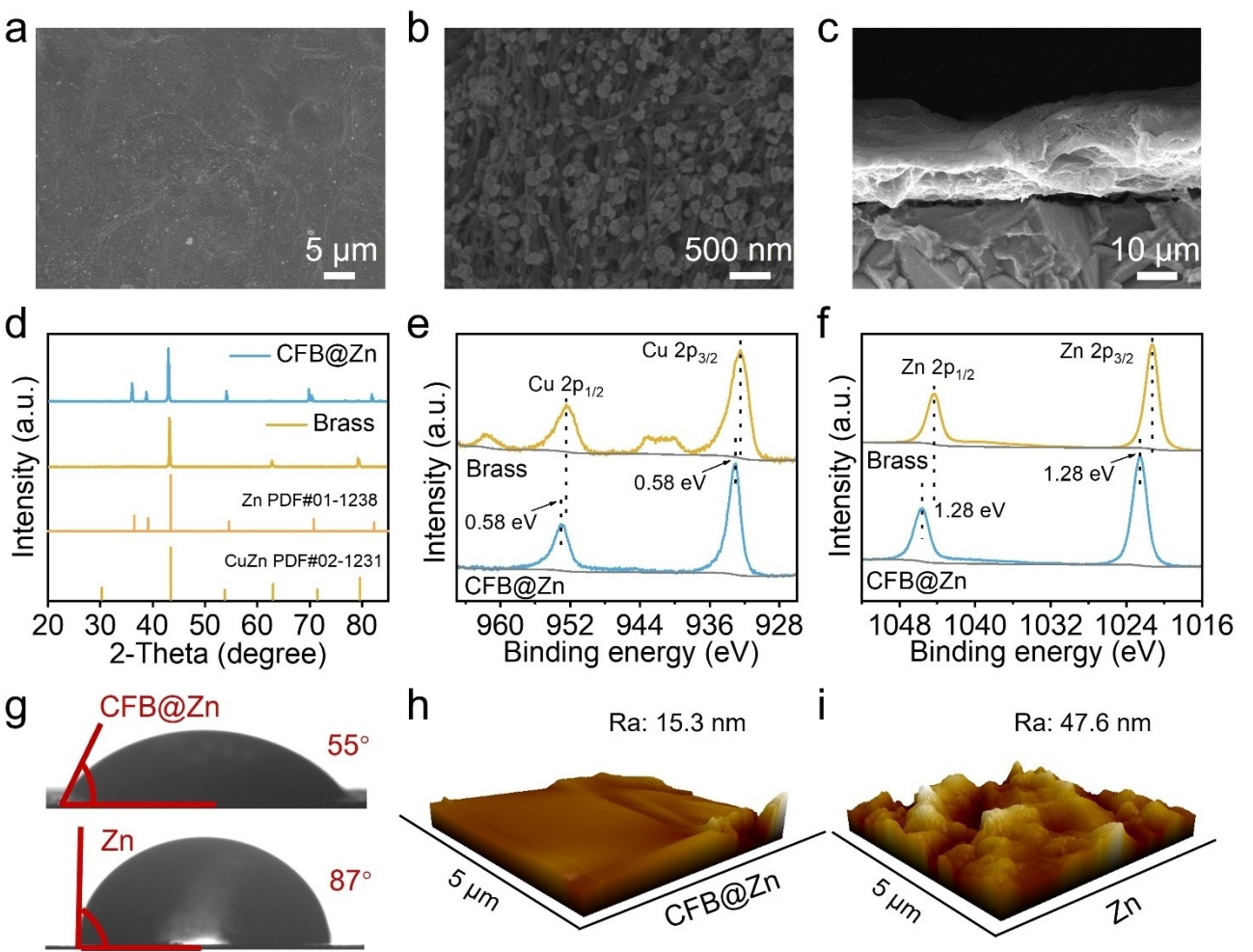


Figure 1. Morphological and structural characterizations of as-prepared interfacial layer. (a, b) Top-view and (c) cross-sectional SEM images of CFB@Zn. (d) XRD patterns of CFB@Zn and commercial brass powder. (e, f) XPS Cu 2p and Zn 2p spectra for CFB@Zn and commercial brass powder. (g) Contact angles of 3 M ZnSO_4 electrolyte on CFB@Zn and bare Zn anodes. (h, i) AFM images of CFB@Zn and bare Zn anodes.

Cu 2p spectra can be attributed to the presence of CuZn species (Figure 1e). Specifically, positive shifts of binding energies (BE) were observed for CFB@Zn as compared to pristine CuZn in the case of both Cu 2p (i.e. 0.58 eV) and Zn 2p (i.e. 1.28 eV) as shown in Figure 1f. This suggested prominent electron transfer from CuZn sites and more importantly, the strong interaction between CuZn and CNT or Zn anode, when establishing the composite interfacial layer.

Enhanced wettability between the CFB@Zn anode and the electrolyte was achieved as shown in Figure 1g. The contact angle of CFB@Zn with 3 M ZnSO_4 solution was 55° , which was decreased as compared to bare Zn (87°). This would contribute to a reduction in charge transfer resistance as well as accelerated transfer of Zn^{2+} at the interface. As further revealed by atomic force microscopy (AFM) in Figure 1h, i and Figure S7, flat and smooth surface features were achieved for CFB@Zn, demonstrating a surface roughness Ra value of 15.3 nm. In contrast, increased fluctuations in the surface height was observed for bare Zn, corresponding to a larger Ra value of 47.6 nm. The reduced surface roughness after introducing the conductive and zincophilic interlayer would effectively weaken

the tip effect, promoting the desired diffusion and deposition behaviors of Zn^{2+} .

The protection role of CFB interlayer against side reactions was first examined by a three-electrode system in 3 M ZnSO_4 electrolyte. By performing the linear polarization tests, the Tafel plots in Figure 2a displayed decreased corrosion current as well as enlarged corrosion potential (-0.959 V) for CFB@Zn as compared to bare Zn (-0.976 V), suggesting enhanced resistance against electrochemical corrosion. After soaking both CFB@Zn and bare Zn anodes in 3 M ZnSO_4 for 3 days, both the surface morphology and composition changes were studied. SEM images indicated that corrosion pits as well as irregular flakes from by-products were generated on the surface of bare Zn, while CFB@Zn anode remained clean and smooth (Figure S8). As further revealed by XRD in Figure 2b, the emerging peaks at around 8° , 16° and 24° corresponded to the formation of by-products (i.e. $\text{Zn}_4\text{SO}_4(\text{OH})_6 \cdot 5\text{H}_2\text{O}$) on bare Zn. On the contrary, the presence of CFB interlayer obviously improved the corrosion-resistance. Linear sweep voltammetry (LSV) curves were also obtained to evaluate the ability of CFB interlayer to suppress H_2 evolution as shown in Figure 2c. As expected,

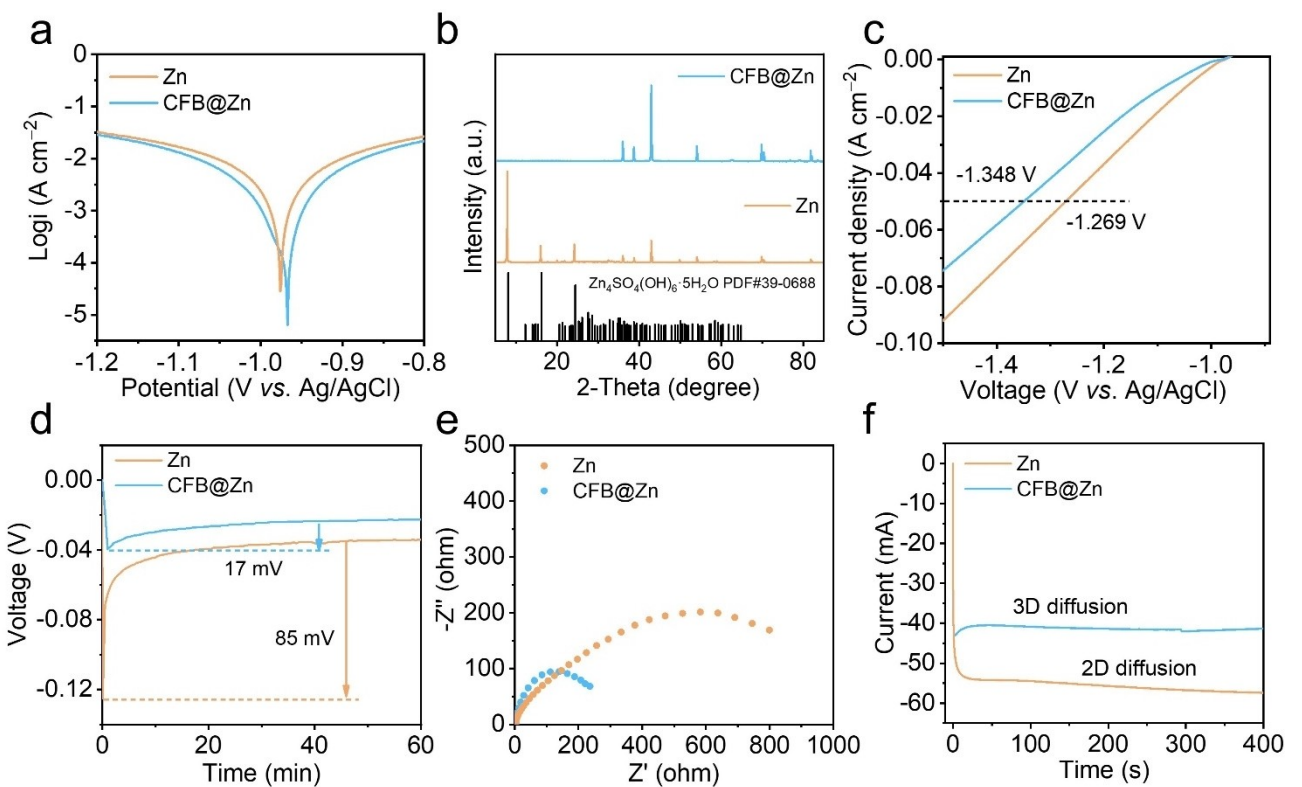


Figure 2. (a) Tafel curves showing corrosion behavior on CFB@Zn and bare Zn anodes. (b) XRD patterns of CFB@Zn and bare Zn anodes after immersing in 3 M $ZnSO_4$ electrolyte. (c) LSV curves of CFB@Zn and bare Zn anodes at 5 mVs^{-1} . (d) Voltage–time curves during Zn nucleation on CFB@Zn and bare Zn anodes. (e) EIS of the symmetric cells before cycling in the frequency range of 100 kHz to 10 mHz; (f) CA study on CFB@Zn and bare Zn at -150 mV overpotential.

CFB@Zn anode exhibited smaller current densities over the entire potential range. Especially at a current density of 50 mA cm^{-2} , the HER overpotential of the CFB@Zn anode was 79 mV higher than that of the bare Zn anode. The CFB interlayer demonstrated considerable protection for Zn anodes against HER as compared with previous literatures (Table S1).

Moreover, $Zn||Zn$ and $CFB@Zn||CFB@Zn$ symmetric cells were assembled and the polarization voltage curves of the first cycle at 1 mA cm^{-2} were displayed in Figure 2d. A significantly reduced nucleation overpotential was achieved for CFB@Zn (17 mV) as compared with bare Zn (85 mV). This can be attributed to the superior zincophilicity of CuZn species and uniform networking morphology of the interfacial layer, which ensured reduced nucleation energy barrier as well as uniform Zn deposition. Similar results were also obtained in the case of the higher current density of 3 mA cm^{-2} (Figure S9). Electrochemical impedance spectra (EIS) were further recorded for symmetric cells based on both bare Zn and CFB@Zn anodes (Figure 2e). Apparently, CFB@Zn manifested a smaller semicircle at the high-frequency region, corresponding to a much lower charge transfer resistance of 272.6Ω than bare Zn (927.3Ω), which was fitted according to the equivalent circuit in Figure S10. A comparison for charge transfer resistance of symmetric cells based on CFB@Zn and recently reported literatures of artificial interface strategies was provided in Table S2. This indicated faster electron transfer across the

CFB@Zn interface, contributing to boosted deposition kinetics of Zn^{2+} . As indicated by chronoamperometry (CA) curves at -150 mV in Figure 2f, a continuous increase in the current response was noticed for bare Zn, suggesting a typical 2D diffusion process towards uneven Zn dendrite growth. With the presence of CFB interlayer, the 2D diffusion of Zn^{2+} terminated in only 30 s, followed by a 3D diffusion pattern at a stabilized current response (ca. -40 mA). During the deposition process, the Zn^{2+} at the CFB@Zn interface was first reduced to metallic Zn atoms, which would then readily absorb on the zincophilic CuZn sites, resulting in restrained 2D diffusion as well as regulated Zn deposition.

The electrochemical reversibility was further characterized by Coulombic efficiency (CE) of Zn plating/stripping with $Zn||Cu$ and $Zn||CFB@Cu$ asymmetric cells at 2 mA cm^{-2} in Figure 3a. After the initial activation for around 10 cycles, the CE reached 99.1% in the case of CFB with barely fluctuation over 700 cycles. In sharp contrast, poor reversibility with rather limited cycle life of less than 100 cycles was noticed for bare Zn. As revealed by the corresponding voltage-capacity profiles in Figure 3b and c, the asymmetric cell based on the CFB interlayer exhibited a smaller voltage gap of ca. 60 mV and can be well retained even after 700 cycles, surpassing that of bare Zn (ca. 90 mV). This was also evaluated in terms of kinetic advantages by performing Zn plating/stripping on Ti foils (Figure 3d). The typical cyclic voltammetry (CV) curves display-

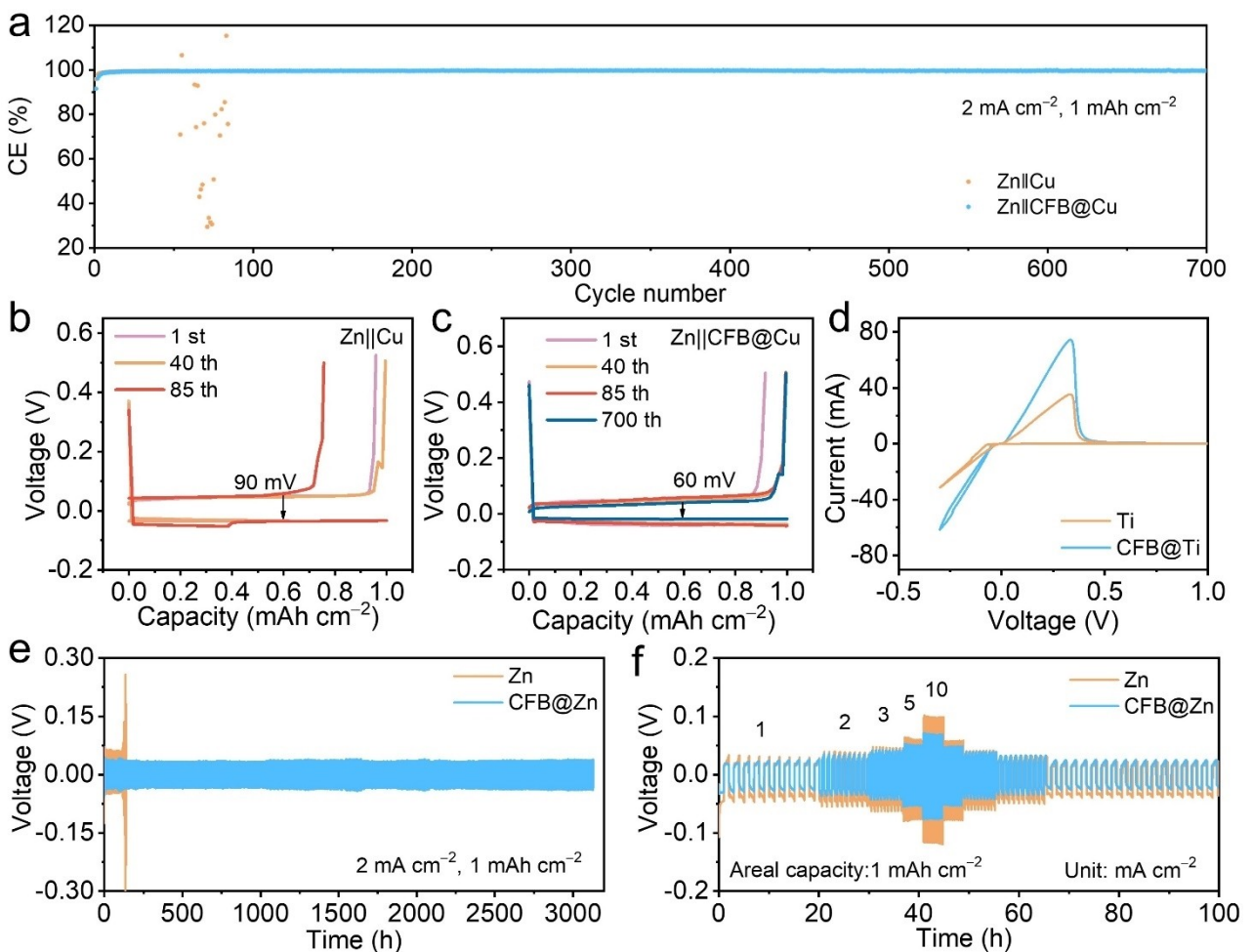


Figure 3. (a) Coulombic efficiency of $\text{Zn} \parallel \text{Cu}$ and $\text{Zn} \parallel \text{CFB@Cu}$ asymmetric cells at 2 mA cm^{-2} with a capacity of 1 mAh cm^{-2} . (b, c) Corresponding voltage profiles at different cycles for $\text{Zn} \parallel \text{Cu}$ and $\text{Zn} \parallel \text{CFB@Cu}$, respectively. (d) CV profiles for Zn nucleation on Ti foil with and without the presence of CFB interlayer. (e) Long-term cycling performance of symmetric cells based on bare Zn and $\text{Zn} \parallel \text{CFB@Zn}$ anodes with a capacity of 1 mAh cm^{-2} at 2 mA cm^{-2} . (f) Rate performance of symmetric cells based on bare Zn and $\text{Zn} \parallel \text{CFB@Zn}$ anodes at different current densities.

ing cathodic loops and anodic peaks corresponded to Zn deposition and Zn dissolution, respectively. Specifically, a shorter delay of cathodic current from the crossover point was achieved with the presence of CFB interlayer (-0.0377 V / -0.0198 V) as compared to bare Zn (-0.0633 V / -0.0160 V), suggesting a reduced Zn deposition barrier.

Furthermore, the Zn plating/stripping performance with CFB was evaluated based on symmetrical Zn batteries at 2 mA cm^{-2} with a fixed areal capacity of 1 mAh cm^{-2} (Figure 3e). Notably, the CFB@Zn anode achieved ultra-long cycling performance for more than 3000 h with a polarization voltage of 33 mV. In contrast, the bare Zn anode persisted for less than 200 h before short circuit. A similar trend was observed at a higher current density of 5 mA cm^{-2} for 1 mAh cm^{-2} (Figure S11), where 8-fold lifespan was delivered by CFB@Zn symmetrical cell as compared to the case of bare Zn. In addition, symmetric cells based on Brass@Zn and CNT@Zn were also assembled and tested at 1 mA cm^{-2} for 1 mAh cm^{-2} (Figure S12). Prominent fluctuations accompanied with short circuits occurred for CNT@Zn after less than 100 h of cycling.

On the contrary, the CFB@Zn anode maintained a low polarization voltage up to 25 mV for over 1800 h, demonstrating the synergy of CNT and CuZn of the interphase layer towards stabilized Zn anode. SEM and XRD analysis after cycling at 1 mA cm^{-2} and 1 mAh cm^{-2} for 40 h also revealed the indispensable role of CFB interlayer in stabilizing Zn anode (Figure S13 and S14). Besides, improved cycling stability was delivered by CFB@Zn at a higher current density of 3 mA cm^{-2} and a capacity of 3 mAh cm^{-2} (Figure S15). Figure 3f displayed the rate performance of symmetric cells based on CFB@Zn and bare Zn anodes. At different current densities (1, 2, 3, 5, 10 mA cm^{-2}), the CFB@Zn anode exhibited smaller polarization voltage throughout the cycling process. In addition, the cycling performance of the CFB@Zn symmetric battery was compared with that of other anodes based on interfacial layers reported in recent literatures (Table S3). It is worth noting that the CFB@Zn anode exhibited outstanding performance in polarization voltage and cycle life under different conditions.

Zn deposition under the current density of 10 mA cm^{-2} was visualized by SEM images with an electrolytic cell. With the Zn

deposition of 5 mAh cm^{-2} , a large number of vertical Zn deposits appeared on the surface of bare Zn (Figure 4a, b). When the the Zn deposition capacity reached 10 mAh cm^{-2} , larger Zn flakes were observed (Figure 4c, d), which would likely evolve into dendrite growth during the repeated Zn plating/stripping. Meanwhile, the surface morphology with the presence of CFB interlayer was presented in Figure 4e–h. Accordingly, a rather flat and dense feature was readily achieved at 5 mAh cm^{-2} . While some uneven Zn deposits such as thin sheet edges in a small area were noticed for 1 h of Zn deposition, the surface still remained compact and relatively uniform, and the dendritic growth was significantly inhibited with no obvious by-products or protrusions. More importantly, the deposition behavior of Zn^{2+} and dynamic evolution of surface morphology at the bare Zn and CFB@Zn anodes was observed by in situ optical microscopy. As shown in Figure 4i, irregular protrusions began to appear on the surface of the bare Zn anode due to the uneven Zn deposition, which evolved into uncontrollable Zn dendrites with the increasing deposition time. This can be ascribed to the tip effect and the gradually deteriorated distribution of interfacial electric field. By contrast, undesirable volume expansion from the cross-sectional view was effectively restrained after introducing the CFB interlayer (Figure 4j). The

uniform increase in thickness was achieved with prolonged deposition time, bits of roughened positions retained stable without evolving into harsh dendrites after 50 min though.

Full cells were also assmebled by coupling Zn anodes with the commercial MnO_2 cathode to evaluate the practical feasibility. Figure 5a shows that the CV curves of the CFB@Zn || MnO_2 cell were similar to those of Zn || MnO_2 cell at 0.1 mV s^{-1} . Clearly, CFB@Zn || MnO_2 exhibited two pairs of redox peaks, i.e. typical cathodic peaks (ca. 1.38 V and 1.24 V) and anodic peaks (ca. 1.58 V and 1.62 V). These can be attributed to the identical two-step redox process of the $\text{Zn}^{2+}/\text{H}^+$ insertion/extraction reactions with MnO_2 . Apart from larger current values, peak shifts during cathodic/anodic scans indicated smaller peak separation and reduced voltage polarization in the case of CFB@Zn || MnO_2 than Zn || MnO_2 full cells, which can be ascribed to enhanced kinetics and promoted reversibility due to the presence of CFB interlayer during the discharge/charge process. Meanwhile, the long-term cycling stability of CFB@Zn || MnO_2 was also examined (Figure 5b). A higher capacity retention of 60.2% after 1000 cycles was achieved by CFB@Zn || MnO_2 , surpassing Zn || MnO_2 (37.5%) at a current density of 2 A g^{-1} . Meanwhile, the discharge specific capacity of CFB@Zn || MnO_2 full cell was higher than that of bare Zn || MnO_2 . EIS tests

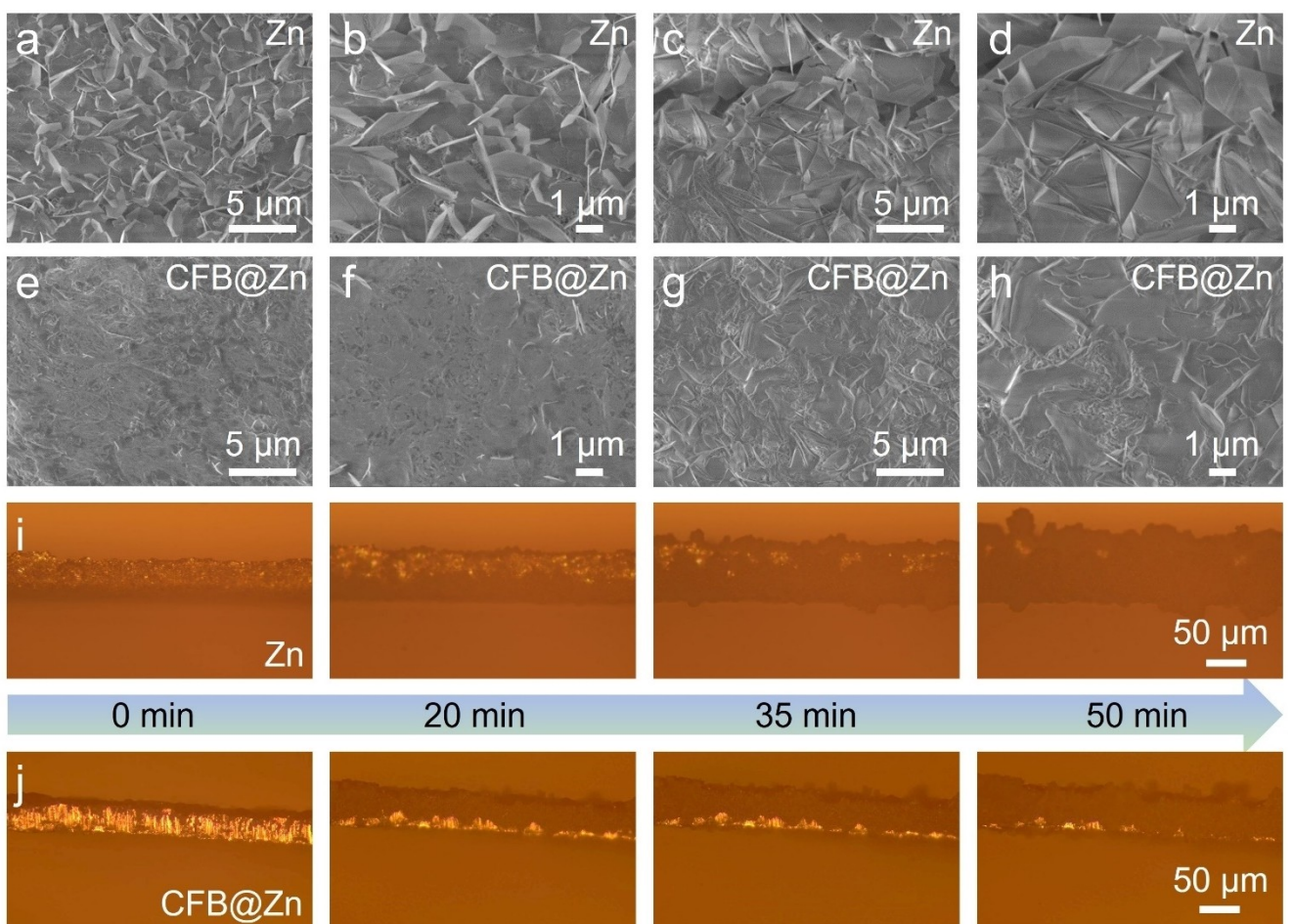


Figure 4. Morphology evolution during Zn deposition at 10 mA cm^{-2} . (a, b) 0.5 h and (c, d) 1 h of Zn^{2+} deposited on bare Zn characterized by SEM. (e, f) 0.5 h and (g, h) 1 h of Zn^{2+} deposited on CFB@Zn characterized by SEM. (i, j) In situ optical images of Zn deposition with and without CFB interlayer.

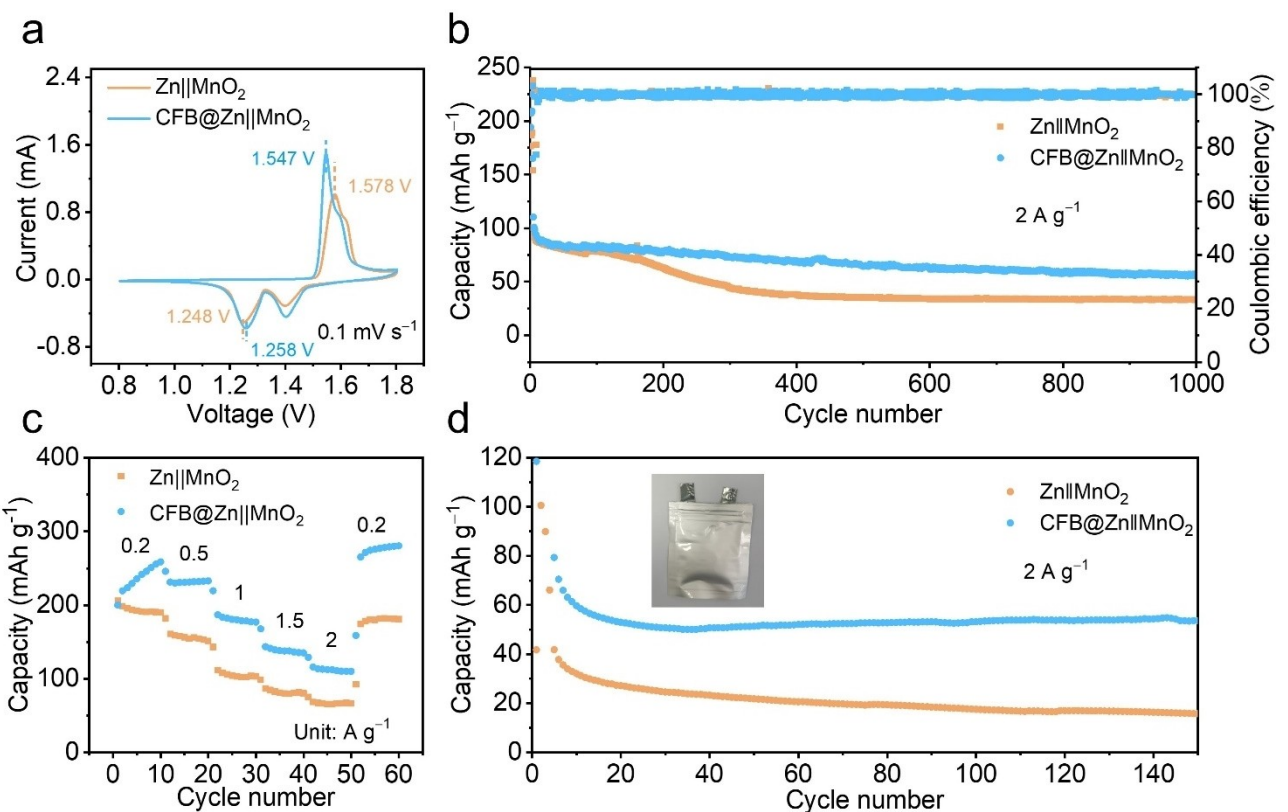


Figure 5. Electrochemical performance of CFB@Zn||MnO₂ full cells compared with bare Zn||MnO₂. (a) CV curves at 0.1 mVs⁻¹. (b) Long-term cycling performance at 2 A g⁻¹. (c) Rate performance at different current densities. (d) Cycling stability of pouch cells at 2 A g⁻¹.

were carried out on the full cells after 50 cycles (Figure S16 and S17). Compared with the charge transfer resistance of Zn (Rct: 29.68 Ω), CFB@Zn had a smaller resistance value (Rct: 2.69 Ω). In addition, the rate capabilities of CFB@Zn||MnO₂ and Zn||MnO₂ full cells at different current densities from 0.2 to 2 A g⁻¹ were explored (Figure 5c). The specific capacities of CFB@Zn||MnO₂ at 0.2, 0.5, 1, 1.5, and 2 A g⁻¹ were 219, 231, 186, 144, and 116 mAh g⁻¹, respectively, which were higher than those of Zn||MnO₂ (195, 155, 106, 81, and 67 mAh g⁻¹). To reveal the versatility of CFB interfacial layer in protecting large-area Zn metal anodes, a quasi-solid-state pouch cell was assembled as shown by the inset photograph in Figure 5d. After the initial activation of five cycles, the CFB@Zn||MnO₂ pouch cell delivered a specific capacity of 70 mAh g⁻¹ at 2 A g⁻¹ and a capacity retention of 75.7% after 150 cycles. By comparison, an inferior capacity of 38 mAh g⁻¹ was achieved by Zn||MnO₂ pouch cell, which faded to merely 16 mAh g⁻¹ (a capacity retention of 42%) accordingly.

Conclusions

In summary, a facile and scalable solvent casting strategy was employed to realize the protective layer over the Zn anode. The conductive network constructed by interconnected CNTs ensured desired electric field distribution over the entire electrode surface. The brass alloy embedded within the carbon

matrix readily inhibited the aggregation of CNTs, and more importantly, suppressed the chemical corrosion with the electrolyte. Lowered nucleation barriers as well as regulated diffusion behavior were readily achieved for Zn deposition. As a result, the symmetric cells based on CFB@Zn anodes delivered extended cycling life of 3000 h and 1200 h at 2 mA cm⁻² and 5 mA cm⁻² for 1 mAh cm⁻², respectively. Furthermore, the CFB@Zn||MnO₂ full cell exhibited impressive cycling stability for 1000 cycles at 2 A g⁻¹. By incorporating carbon hybrids onto the surface of Zn metal in a straightforward and cost-effective manner, this strategy effectively enhanced interfacial kinetics and enabled a highly reversible anode, offering new possibilities for advancing batteries based on metal anodes.

Acknowledgements

K. Rui and K. Chen contributed equally to this work. This work was financially supported by National Natural Science Foundation of China (51902158), and "Six Talent Peak" Project of Jiangsu Province (XCL-021).

Conflict of Interests

The authors declare no conflict of interest.

Data Availability Statement

The data that support the findings of this study are available from the corresponding author upon reasonable request.

Keywords: Aqueous Zn-ion batteries • Dendrite-free anode • Interfacial protective layer • Carbon hybrids

- [1] a) F. Wang, O. Borodin, T. Gao, X. Fan, W. Sun, F. Han, A. Faraone, J. A. Dura, K. Xu, C. Wang, *Nat. Mater.* **2018**, *17*, 543–549; b) X. Yang, Y. Zhao, S. Lv, L. Zhong, C. Yue, S. Zhan, L. Zhao, C. Wang, X. Li, X. Liu, Z. Tang, C. Zhang, C. Zhi, H. Lv, *Energy Environ. Sci.* **2024**, *17*, 4758–4769.
- [2] a) Y. Cao, Y. Chen, K. Chen, L. Sun, W. Si, Y. Yan, H. Lin, J. Zhu, P. He, Y. Lu, H. Xie, K. Rui, *Chem. Eng. J.* **2024**, *494*, 152863; b) P. Jiang, T. Liu, C. Lei, H. Wang, J. Li, M. Shi, C. Xu, X. He, X. Liang, *J. Am. Chem. Soc.* **2024**, *146*, 25108–25117.
- [3] a) Y. Gao, Q. Cao, J. Pu, X. Zhao, G. Fu, J. Chen, Y. Wang, C. Guan, *Adv. Mater.* **2023**, *35*, 2207573; b) Q. Zhang, J. Luan, X. Huang, L. Zhu, Y. Tang, X. Ji, H. Wang, *Small* **2020**, *16*, 2000929; c) H. Yu, Y. Zeng, N. W. Li, D. Luan, L. Yu, X. W. Lou, *Sci. Adv.* **2022**, *8*, eabm5766.
- [4] a) G. Li, Z. Zhao, S. Zhang, L. Sun, M. Li, J. A. Yuwono, J. Mao, J. Hao, J. Vongsivut, L. Xing, C.-X. Zhao, Z. Guo, *Nat. Commun.* **2023**, *14*, 6526; b) Z. Liu, R. Wang, Y. Gao, S. Zhang, J. Wan, J. Mao, L. Zhang, H. Li, J. Hao, G. Li, L. Zhang, C. Zhang, *Adv. Funct. Mater.* **2023**, *33*, 2308463; c) J. Yin, Y. Luo, M. Li, M. Wu, K. Guo, Z. Wen, *ACS Appl. Mater. Interfaces* **2024**, *16*, 53242–53251; d) L. Yao, J. Liu, F. Zhang, B. Wen, X. Chi, Y. Liu, *Nat. Commun.* **2024**, *15*, 6249; e) G. Yoo, Y.-G. Lee, B. Im, D. G. Kim, Y.-R. Jo, G. H. An, *Energy Storage Mater.* **2023**, *61*, 102845.
- [5] a) Y. Su, B. Liu, Q. Zhang, J. Peng, C. Wei, S. Li, W. Li, Z. Xue, X. Yang, J. Sun, *Adv. Funct. Mater.* **2022**, *32*, 2204306; b) L. Yao, C. Hou, M. Liu, H. Chen, Q. Zhao, Y. Zhao, Y. Wang, L. Liu, Z.-W. Yin, J. Qiu, S. Li, R. Qin, F. Pan, *Adv. Funct. Mater.* **2023**, *33*, 2209301.
- [6] a) J. Jiang, Z. Pan, J. Yuan, J. Shan, C. Chen, S. Li, HaiXu, Y. Chen, Q. Zhuang, Z. Ju, H. Dou, X. Zhang, J. Wang, *Chem. Eng. J.* **2023**, *452*, 139335; b) J.-L. Yang, L. Liu, Z. Yu, P. Chen, J. Li, P. A. Dananjaya, E. K. Koh, W. S. Lew, K. Liu, P. Yang, H. J. Fan, *ACS Energy Lett.* **2023**, *8*, 2042–2050; c) R. Zhao, X. Dong, P. Liang, H. Li, T. Zhang, W. Zhou, B. Wang, Z. Yang, X. Wang, L. Wang, Z. Sun, F. Bu, Z. Zhao, W. Li, D. Zhao, D. Chao, *Adv. Mater.* **2023**, *35*, 2209288; d) S. Zhao, Y. Zhang, J. Li, L. Qi, Y. Tang, J. Zhu, J. Zhi, F. Huang, *Adv. Mater.* **2023**, *35*, 2300195; e) S. Lee, Y. Je, B. Seok, H. T. Kim, Y.-R. Jo, S. Ju Oh, B. Im, D. G. Kim, S.-S. Chee, G.-H. An, *Energy Chem.* **2024**, *92*, 113–123; f) G. Yoo, Y.-R. Jo, G.-H. An, *ACS Energy Lett.* **2024**, *9*, 5955–5965.
- [7] a) X. Zhou, B. Wen, Y. Cai, X. Chen, L. Li, Q. Zhao, S.-L. Chou, F. Li, *Angew. Chem. Int. Ed.* **2024**, *63*, e202402342; b) Q. Ren, X. Tang, X. Zhao, Y. Wang, C. Li, S. Wang, Y. Yuan, *Nano Energy* **2023**, *109*, 108306; c) D. Han, S. Wu, S. Zhang, Y. Deng, C. Cui, L. Zhang, Y. Long, H. Li, Y. Tao, Z. Weng, Q.-H. Yang, F. Kang, *Small* **2020**, *16*, 2001736.
- [8] a) B. Wei, J. Zheng, X. AbhishekLiuLiu, J. Wu, Z. Qi, Z. Hou, R. Wang, J. Ma, A. N. Gandi, Z. Wang, H. Liang, *Adv. Energy Mater.* **2024**, *14*, 2401018; b) P. Liang, J. Yi, X. Liu, K. Wu, Z. Wang, J. Cui, Y. Liu, Y. Wang, Y. Xia, J. Zhang, *Adv. Funct. Mater.* **2020**, *30*, 1908528.
- [9] a) H. Lu, J. Hu, K. Zhang, J. Zhao, S. Deng, Y. Li, B. Xu, H. Pang, *Adv. Mater.* **2024**, *36*, 2309753; b) Z. Zhao, H. Zhang, X. Shi, Y. Zhang, C. Tang, H. Zhao, J. Liu, G. Wang, L. Li, *Small* **2024**, *20*, 2304723; c) C. Guo, J. Zhou, Y. Chen, H. Zhuang, J. Li, J. Huang, Y. Zhang, Y. Chen, S.-L. Li, Y.-Q. Lan, *Angew. Chem. Int. Ed.* **2023**, *62*, e202300125.
- [10] a) Y. Meng, M. Wang, J. Xu, K. Xu, K. Zhang, Z. Xie, Z. Zhu, W. Wang, P. Gao, X. Li, W. Chen, *Angew. Chem. Int. Ed.* **2023**, *62*, e202308454; b) H. He, L. Zeng, D. Luo, J. He, X. Li, Z. Guo, C. Zhang, *Adv. Mater.* **2023**, *35*, 2211498; c) Y. Liu, T. Guo, Q. Liu, F. Xiong, M. Huang, Y. An, J. Wang, Q. An, C. Liu, L. Mai, *Mater. Today Energy* **2022**, *28*, 101056.
- [11] a) T. Huang, K. Xu, N. Jia, L. Yang, H. Liu, J. Zhu, Q. Yan, *Adv. Mater.* **2023**, *35*, 2205206; b) Y. Mu, Z. Li, B.-K. Wu, H. Huang, F. Wu, Y. Chu, L. Zou, M. Yang, J. He, L. Ye, M. Han, T. Zhao, L. Zeng, *Nat. Commun.* **2023**, *14*, 4205.
- [12] a) L. Kang, K. Yue, C. Ma, H. Yuan, J. Luo, Y. Wang, Y. Liu, J. Nai, X. Tao, *Nano Lett.* **2024**, *24*, 4150–4157; b) Y. Zeng, X. Zhang, R. Qin, X. Liu, P. Fang, D. Zheng, Y. Tong, X. Lu, *Adv. Mater.* **2019**, *31*, 1903675; c) L. Dong, W. Yang, W. Yang, H. Tian, Y. Huang, X. Wang, C. Xu, C. Wang, F. Kang, G. Wang, *Chem. Eng. J.* **2020**, *384*, 123355; d) Y. Zhou, J. Xia, J. Di, Z. Sun, L. Zhao, L. Li, Y. Wu, L. Dong, X. Wang, Q. Li, *Adv. Energy Mater.* **2023**, *13*, 2203165; e) H. Heo, K. Yun, G.-H. An, J. Alloys Compd. **2023**, *965*, 171229.
- [13] H. Zhang, L. Yang, H. Wang, B. Cui, J. Wang, X. Han, W. Hu, *Adv. Funct. Mater.* **2024**, *34*, 2312469.
- [14] K. Yun, G.-H. An, *Chem. Eng. J.* **2024**, *479*, 147303.
- [15] a) B. Li, K. Yang, J. Ma, P. Shi, L. Chen, C. Chen, X. Hong, X. Cheng, M.-C. Tang, Y.-B. He, F. Kang, *Angew. Chem. Int. Ed.* **2022**, *61*, e202212587; b) R. Li, Y. Du, Y. Li, Z. He, L. Dai, L. Wang, X. Wu, J. Zhang, J. Yi, *ACS Energy Lett.* **2023**, *8*, 457–476; c) M. Kwon, J. Lee, S. Ko, G. Lim, S.-H. Yu, J. Hong, M. Lee, *Energy Environ. Sci.* **2022**, *15*, 2889–2899; d) Y. Chen, Y. Cao, K. Chen, J. Rui, J. Chang, Y. Yan, H. Lin, Y. Lu, C. Zhao, J. Zhu, K. Rui, *Small* **2024**, *20*, 2401249.

Manuscript received: December 15, 2024

Revised manuscript received: January 18, 2025

Accepted manuscript online: February 5, 2025

Version of record online: February 10, 2025